

Tensional twist-folding of sheets into multilayered architectures and scrolled yarns

Julien Chopin,^{1,2,*} Arshad Kudrolli,^{1,*}

¹Department of Physics, Clark University, Worcester, MA 01610, USA,

²Instituto de Física, Universidade Federal da Bahia, Salvador-BA 40170-115, Brazil

^{*}To whom correspondence should be addressed;

E-mail: julien.chopin@ufba.br (JC); akudrolli@clarku.edu (AK)

Abstract

Twisting sheets as a strategy to form yarns with nested structure lacks scientific guiding principles but relies on millennia of human experience in making catguts, food packaging, and redeployable fabric wearables. We formulate a tensional twist-folding route to making yarns with prescribed folded, scrolled, and encapsulated architectures by remote boundary loading. By harnessing micro-focus x-ray scanning to noninvasively image the fine internal structure, we show that a twisted sheet follows a surprisingly ordered folding transformation as it self-scrolls to form structured yarns. As a sheet is twisted by a half-turn, we find that the elastic sheet spiral accordion folds with star polygon shapes characterized by Schläfli symbols set by the primary instability. A scalable model incorporating dominant stretching modes with origami kinematics explains not only the observed multilayered structure, torque, and energetics, but also the topological transformation into yarns with prescribed crosssections through recursive folding and twist localization. By using hyperelastic materials, we further demonstrate that a wide range of structures can be readily redeployed, going well beyond other self-assembly methods in current broad use.

Significance Statement: We demonstrate a scalable redeployable twisting strategy guided by origami and elasticity to make architectured sheets and yarns. Building on experience gained by humanity in making catgut bow strings and surgical sutures, twisting has been proposed as a method to make functional yarns from ultra-thin materials. However, energy scaling analysis used to understand small-amplitude wrinkling of sheets cannot be extended to the large

deformation regime reached during shape transformations. We discover spiral accordion folding develops and further guides the nesting of the structure even as the sheet compacts into a yarn. We show that the entire shape transformation can be algorithmically described using ancient Greek polygon symbols and rigid origami kinematics starting from the near-threshold energetics.

1 Introduction

Tensional twist-folding is a method to transform flat sheets into layered structures and yarns with ordered internal architectures by remote boundary manipulation. Twisting sheets under tension has been used since antiquity in making catgut bow strings, surgical sutures, musical chord instruments, sports rackets, sausage and candy wrappers, fabric filters and wearables such as turbans and crushed dupattas, and in upcycling of plastic (Fig. 1a to c). Scrolled yarns nested structures optimized for energy harnessing, batteries, and embedding materials [1, 2, 3, 4] are difficult to achieve by compression-induced transformations of elastic sheets [5, 6, 7], and traditional fiber spinning methods [8]. Being topological, they can be fully reversible when appropriate materials are used, and can be repurposed and redeployed, as exemplified by the multifunctional Rajasthani turban. Nevertheless, the fundamental transformations beyond the perturbative regime near the unstressed configuration [9, 10, 11, 12, 13, 14, 15, 16, 17] have not been documented when extreme deformation and self-contact develop, let alone calculated as in slender rods and ribbons [18, 19, 20, 21]. Origami and inextensible sheet models are amenable to address large shape transformations while crumpling, folding, and capillary wrapping [22, 23, 24, 25, 26, 27, 28, 29, 30, 31, 32, 33], but their application to sheets which can stretch significantly is unclear. Here, we demonstrate that symmetric accordion folded structures can be obtained by a tensional twist-folding model that compounds geometry and elastic theory and can serve as a guide for fabrication of yarns with precise control of crosssectional architecture.

2 Results

2.1 Ordered transformation in tensional twist-folded sheets

Examples of a polydimethylsiloxane (PDMS) sheet with increasing twist are shown in Fig. 1d to g and Movie S1. The system consists of a sheet of length L , width W , and thickness t , twisted by an angle θ while being held at opposite ends and stretched axially by ΔL (Fig. 1d, inset). Transverse wrinkles can be observed just above the onset of primary instability (Fig. 1d), which grow in amplitude and collapse into a star-shaped accordion folded spiral structure with self-contact (Fig. 1e). As θ is increased further, a nestled helical structure forms at the waist (Fig. 1f), before a secondary instability occurs which leads to recursive folding and a scrolled yarn (Fig. 1g). Each of the major shape transformations causes the rate of change of applied torque M to change sign, leading to a sawtooth variation with twist (Fig. 1h). The primary instability and parameter space over which these transformations occur varies with L/W (Fig. 1i). While the observed primary instabilities are consistent with the clamp-dominated ($L \sim W$) and the ribbon ($L \gg W$) regimes, which scale as $\theta_p \sim (L/W)^\zeta$, with $\zeta = 1$ and 2, respectively, and wavelength $\lambda_p \sim \sqrt{Lt}(\Delta L/L)^{-1/4}$ [13, 16], the self-contact and secondary instability are documented and analyzed here for the first time.

2.2 Curvature localization, stored elastic energy, and nonmonotonic torque

Using noninvasive 3D x-ray tomography, we reconstruct the central 80% of a twisted Poly-Vinyl Siloxane (PVS) sheet and calculate its mean curvature H (Fig. 2a and Methods in the supplementary materials), and note high-curvature regions along wrinkle antinodes which develop above the onset of transverse instability. To recognize the spatial distribution of the curvature as the sheet wraps around itself, we mapped H to a rectangular domain (Fig. 2b to e). The wrinkles are observed to be aligned with the applied tension when $\theta = 90^\circ$ consistent with linear perturbation analysis [13]. With increasing twist, H is increasingly localized along folds with

essentially flat regions in between, and the folds rotate away from the tensional axis till they meet near the clamped edges.

We calculate the bending energy density $w_b = B/2 (H^2 + 2(1 - \nu)K)$, where $B = Y t^3/[12(1 - \nu^2)]$ is the bending stiffness, ν the Poisson ratio, K the Gaussian curvature, and Y the Young's modulus. Plotting w_b across the sheet at mid-distance between the clamps, we observe that sharp peaks grow with θ showing that the bending energy increasingly localizes along the folds (Fig. 2f). Because the number of the peaks is unchanged as twist is increased, we postulate that the number of folds n are set by twice the ratio of W and λ_p . Accordingly, we plot the observed n versus the predicted $n = 2W/\lambda_p$ (Fig. 2g), and observe good agreement.

2.3 Scalar Model

Based on these observations, we have developed a scalar model to compute the torsional response and stored elastic energy of the sheet as a function of applied twist (see Elastic Energy Scalar Model in the supplementary materials). We assume that the sheet deformation is predominantly given by elongation along straight lines as represented by the red and blue lines connecting the clamped edges and the central crosssection. The complex kinematics of the central crosssection is assumed to be captured by the normalized parameter $\chi = D/W$, where D is the diameter of a circle enclosing the central sheet crosssection (Fig. 2j and Fig. S6). Then, the measured and calculated values of $M(\theta)$ are plotted in Fig. 2k following the derivations of our model. In contrast with M calculated using the Föppl-von Kármán (FvK) equations [9, 34], which predict an ever increasing torque with twist, our scalar elastic model captures the non-monotonic torsional response quantitatively till the onset of self-contact.

In Fig. 2h, we compare the measured (circles) and calculated elastic energy (solid black line) scaled by \mathcal{E}_0 as a function of twist. We find very good agreement showing that the bending energy can be neglected (Fig. 2i). It is noteworthy that, while the bending energy contribution

to the elastic energy is small, folding is necessary to achieve a net energy reduction. To demonstrate this, we have plotted the helicoidal elastic energy ($\chi = 1$) in Fig. 2h (dashed line). The energy is observed to grow well above the elastic energy of a folded sheet ($\chi < 1$), showing that folding clearly results in a lower growth in the elastic energy.

We next discuss a geometric model based on origami construction to explain the folded structure which develops after a half-turn. Consider an inextensible sheet (Fig. 3a) which can be folded up or down along the dashed lines, which results in a star-shaped polygonal spiral origami (Fig. 3b). The apex angle of the isosceles triangular folds is α . An image of an elastic sheet with the same aspect ratio is shown in Fig. 3c, where the thickness of the sheet has been chosen such that it results in the same number of folds as in the origami. We plot the segment angle β from the \bar{y} -axis made by initial horizontal lines in Fig. 3d. Quantitative agreement is found away from the clamps with the expected value assuming solid body rotation of the triangles, where each fold acts as a hinge. We also measure α from shadowgraph images and find that it decreases with strain $\Delta L/L$ (Fig. 3e). This variation occurs because the length increases with applied strain resulting in a linear decrease in subtended angle to leading order (dashed line). Thus, good agreement can be observed between the origami shape and the twisted sheet away from the clamped edges. Further quantitative agreement can be observed with physical cuts mid-way between the clamps (see Transect Cut Comparisons in the supplementary materials).

2.4 Schläfli origami and layered architectures at half-turn

Origami corresponding to spiral accordion folded elastic sheets can be algorithmically generated using α as a parameter. Consider a right angle triangle with height L and angle $\alpha/2$ (Fig. 4a). (This triangle is also the same as that at the far left side of the sheet in Fig. 4a.) To help understand the geometrical transformation leading to a flat folded origami, we preserve

the color when reflecting off a right triangle with respect to its height, and change color when reflecting the triangle with respect to its hypotenuse identified as a fold. A flat-fold origami is thus obtained by applying alternately these two transformations until reaching a given number of folds n . For specific values of α , these transformations result in a regular flat-folded origami where the triangle bases are the edges of a regular polygon with p vertices (Fig. 4a). This polygon is also the convex envelop of a star-shaped polygon composed by the hypotenuses (dashed black line) connecting vertices separated by q consecutive triangle bases (solid orange line). These origami can be identified by the so-called Schläfli symbols p, q , and thus we name them *Schläfli origami*. Varying the Schläfli symbols (or equivalently reducing the tip angle and increasing the triangle numbers,) one can obtain triangle, pentagon, heptagon, and nonagon shaped envelops. The thickness of the overlapped regions at the center is given by $t' = nt$ and decreases in integer multiples of t toward the edges.

In Fig. 4b, we show in the first column flat-folded Schläfli origami of higher symmetry, and in the second column their incomplete counterparts obtained by restricting the number of folds to $n = 2 W/\lambda_p$, keeping p the same. The examples in the 1st, 3rd, and 4th row are symmetric, and the one in the 2nd row is asymmetric, and thus a Schläfli origami with either symmetry can be generated according to our algorithm by starting with a right angle triangle reflecting about the hypotenuse and height equal to the calculated number of folds. Partial Schläfli origami have been denoted with color intensity which is proportional to the number of overlapping domains at the particular location. They can be compared with radiograms of spiral folded elastic sheets which have the same L/W and n (third column). The color map in the radiogram is linearly proportional to absorption encountered along the linear path of the x-rays, and thus can be observed to be consistent with those generated by origami.

The correspondence can be further quantified by measuring from the radiograms the fold angle ψ and α , after a 180° twist (Fig.4c to e). α does not vary significantly between the

triangles of a given twisted sheet, in accordance with the predictions of the Schläfli origami (Fig.4e). We find an excellent agreement without any fit parameters for all three measures. Thus, the orientation of the folds is given by our model, which neglects the elastic stretching of the sheet, and reveals the strong connection between twisted sheets, classical Greek geometry and origami.

2.5 Twist localization and topological transformation into scrolled yarns

Fig. 5a to c shows radiograms of a twisted sheet with increasing twist next, where the tracked edges of the sheet are marked to depict how the twist localizes itself increasingly away from the clamped edges. A set of transects at $\bar{x}/L = 0.5, 0.55$, and 0.8 for $\theta = 180^\circ, 360^\circ$, and 720° are shown in Fig. 5d to show the internal structure of the fan and yarn sections, where the sheet edges are also denoted with corresponding red and blue markers. The central helical yarn section undergoes strong compaction resulting first in a nested helicoid ($\bar{x}/L = 0.5, 0.55$ for $\theta = 360$ deg), and then a recursive folding when the secondary instability occurs at θ_s . Encapsulated regions whose number increases with twist, and with a maximum at $\bar{x} = L/2$, are highlighted by the magenta shade. The χ before and after this secondary instability (denoted by the vertical line) is plotted as a function of L/W for various $\Delta L/L$ in Fig. 5e. We observe that the ratio is 2 in all cases, showing a recursive folding of the sheet.

One then infers from these radiograms and transects that the sheet can be divided into three sections with a yarn-like structure in the center of length L_Y , and two fan-like structures near the clamped edges characterized by fan angle ϕ (see the inset to Fig. 5f). To quantify these regions, we use the orientation of the segment joining the end-points in the $y - z$ plane to obtain a crosssection orientation angle θ_x (Fig. 5d and Fig.S10). We plot θ_x in Fig. 5f after the sheet is twisted twice, and find that the twist is localized in the central section, where the local twisting rate θ_x/L_Y is approximately 4 times greater than θ/L .

We obtain the evolution of L_Y and ϕ with twist over various L/W . As evidenced by a good collapse of the experimental data on a master curve in Fig. 5g, we find that L_Y grows as $\chi(\theta - \theta_s)/(1 - \chi)$. We develop a geometric yarn model based on the kinematics of the sheet edge with θ . Using trigonometry rules (see Yarn Model in the supplementary materials), we derive a theoretical fan angle $\phi_{th} = (W - D)/(L - L_Y)$ which is observed to be in good agreement with the measured one (Fig. 5h). Assuming that the helical angle of the yarn is imposed by ϕ (Fig. S11A), the yarn growth rate with twist $dL_Y/d\theta$ is given by the twist rate ϕ/D , which is a decreasing function of L_Y modeled by a linear first-order ODE whose solution is $L_Y/L = 1 - \exp(-\Theta/2)$, where $\Theta = \chi(\theta - \theta_s)/(1 - \chi)$. Considering that there are no adjustable parameters, this exponential growth model is in very good agreement with experimental data shown in Fig. 5h. While this growth appears to impose a maximum yarn length L , one can obtain an arbitrary long yarn by changing one of the clamped ends with two rollers which feed in more material.

3 Discussion

In conclusion, we have demonstrated with experiments and our tensional twist-folding model that a flat sheet follows a remarkably ordered route to yarns with delicate nested structures which can be algorithmically generated using Schläfli symbols and rigid origami kinematics. We show the key role of sheet stretchability and applied tension to select the fold number and organize the folding into tightly scrolled yarns. Unlike other twist-less transformations where only the surface is modified, recursive folding and twist localization in the yarn regime offers a new strategy to control and adjust the yarn crosssection. Our study will serve as a scientific guide to describing large shape transformation of elastic sheets into twisted multilayered architectures.

References

- [1] C. H. Kwon, *et al.*, *Nat. Commun.* **5**, 1 (2014).
- [2] M. D. Lima, *et al.*, *Science* **331**, 51 (2011).
- [3] R. Cruz-Silva, *et al.*, *ACS nano* **8**, 5959 (2014).
- [4] Z. Xu, H. Sun, X. Zhao, C. Gao, *Adv. Mater.* **25**, 188 (2013).
- [5] A. Lobkovsky, S. Gentges, H. Li, D. Morse, T. A. Witten, *Science* **270**, 1482 (1995).
- [6] L. Pocivavsek, *et al.*, *Science* **320**, 912 (2008).
- [7] J. L. Silverberg, *et al.*, *Science* **345**, 647 (2014).
- [8] J. W. S. Hearle, P. Grosberg, S. Backer, *Wiley-Interscience* (1969).
- [9] A. E. Green, *Proc. R. Soc. London Ser. A* **161**, 197 (1937).
- [10] B. Davidovitch, R. D. Schroll, D. Vella, M. Adda-Bedia, E. A. Cerdá, *Proc. Natl. Acad. Sci. USA* **108**, 18227 (2011).
- [11] H. Vandeparre, *et al.*, *Phys. Rev. Lett.* **106**, 224301 (2011).
- [12] J. Chopin, A. Kudrolli, *Phys. Rev. Lett.* **111**, 174302 (2013).
- [13] J. Chopin, V. Démery, B. Davidovitch, *J. Elast.* **119**, 137 (2015).
- [14] D. Vella, J. Huang, N. Menon, T. P. Russell, B. Davidovitch, *Phys. Rev. Lett.* **114**, 014301 (2015).
- [15] J. Chopin, A. Kudrolli, *Soft Matter* **12**, 4457 (2016).
- [16] A. Kudrolli, J. Chopin, *Proc. R. Soc. Ser. A* **474**, 20180062 (2018).

[17] A. Panaitescu, M. Xin, J. Chopin, B. Davidovitch, A. Kudrolli, *Phys. Rev. E* **100**, 053003 (2019).

[18] G. H. M. Van der Heijden, S. Neukirch, V. G. A. Goss, J. M. T. Thompson, *Int. J. Mech. Sci.* **45**, 161 (2003).

[19] O. O. Kit, T. Tallinen, L. Mahadevan, J. Timonen, P. Koskinen, *Phys. Rev. B* **85**, 085428 (2012).

[20] N. Charles, M. Gazzola, L. Mahadevan, *Phys. Rev. Lett.* **123**, 208003 (2019).

[21] V. P. Patil, J. D. Sandt, M. Kolle, J. Dunkel, *Science* **367**, 71 (2020).

[22] M. B. Amar, Y. Pomeau, *Proc. R. Soc. Lond. Ser. A* **453**, 729 (1997).

[23] E. Cerdà, S. Chaieb, F. Melo, L. Mahadevan, *Nature* **401**, 46 (1999).

[24] E. Hamm, B. Roman, F. Melo, *Phys. Rev. E* **70**, 026607 (2004).

[25] D. L. Blair, A. Kudrolli, *Phys. Rev. Lett.* **94**, 166107 (2005).

[26] G. W. Hunt, I. Ario, *Int. J. Nonlin. Mech.* **40**, 833 (2005).

[27] C. Py, *et al.*, *Phys. Rev. Lett.* **98**, 156103 (2007).

[28] A. P. Korte, E. L. Starostin, G. H. M. van der Heijden, *Proc. R. Soc. London Ser. A* **47**, 285 (2010).

[29] H. Diamant, T. A. Witten, *Phys. Rev. Lett.* **107**, 164302 (2011).

[30] C. D. Santangelo, *Annu. Rev. Condens. Matter Phys.* **8**, 165 (2017).

[31] S. J. P. Callens, A. A. Zadpoor, *Mater. Today* **21**, 241 (2018).

[32] D. Kumar, J. D. Paulsen, T. P. Russell, N. Menon, *Science* **359**, 775 (2018).

[33] J. D. Paulsen, *Annu. Rev. Condens. Matter Phys.* **10**, 431 (2019).

[34] J. Chopin, R. T. D. Filho, *Phys. Rev. E* **99**, 043002 (2019).

Acknowledgments: We thank Andreea Panaiteescu for help with preliminary experiments, and Benjamin Allen and Fabio Lingua for setting up the x-ray system. We thank Madelyn Leembruggen, Benoit Roman, and Joseph Paulsen for their critical reading of the manuscript and their comments. **Funding:** The work at Clark University was supported by U.S. National Science Foundation grants DMR-1508186 and DMR-2005090; **Author contributions:** JC and AK designed research, conducted experimental and theoretical research, and wrote the paper.

Competing interests: The authors declare no competing interests. **Data and materials availability:** All data are available in the main text or the supplementary materials.

Supplementary materials

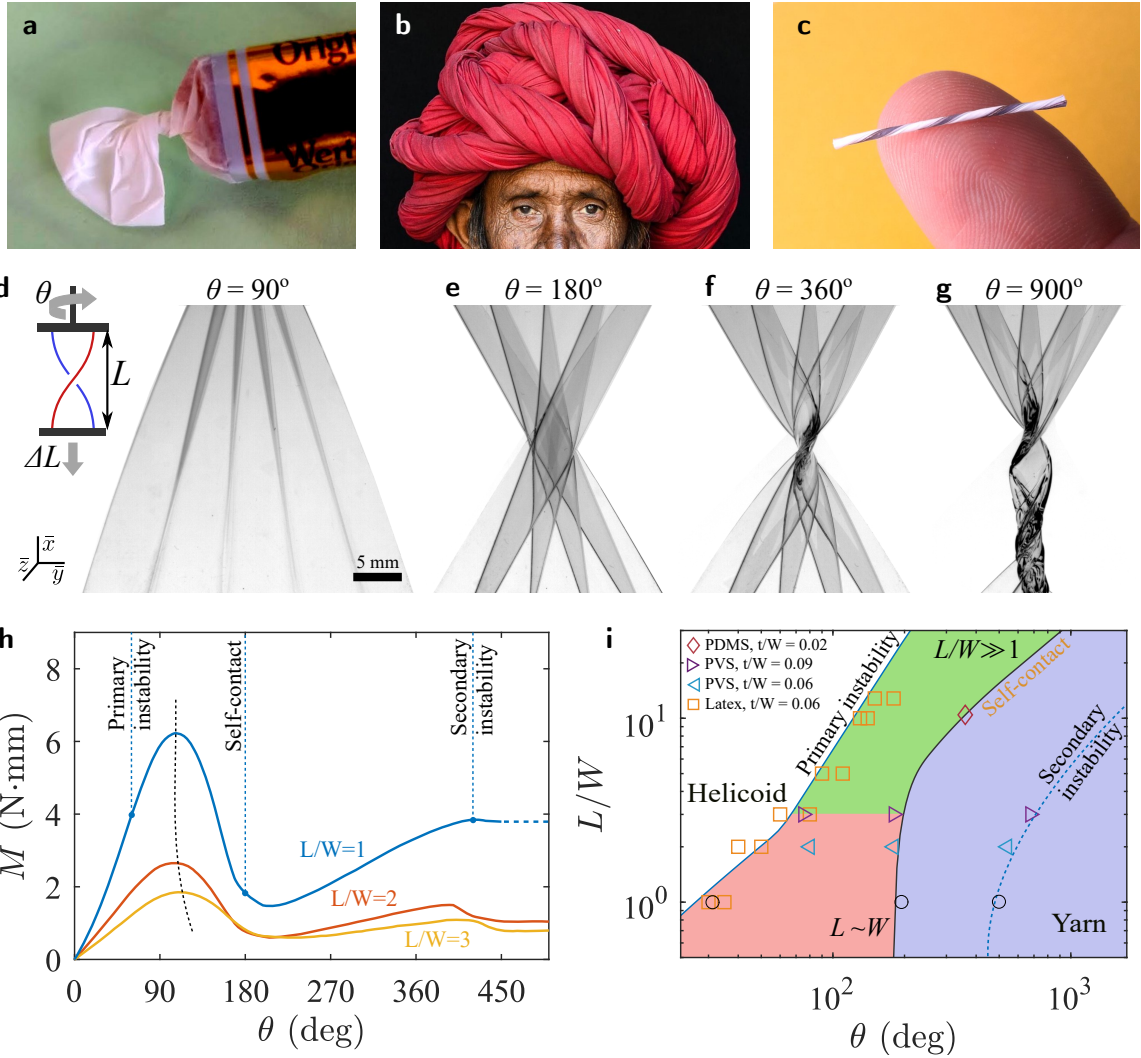
Materials and Methods

Figs. S1 to S11

Tables S1 and S2

Movie S1

References (35)



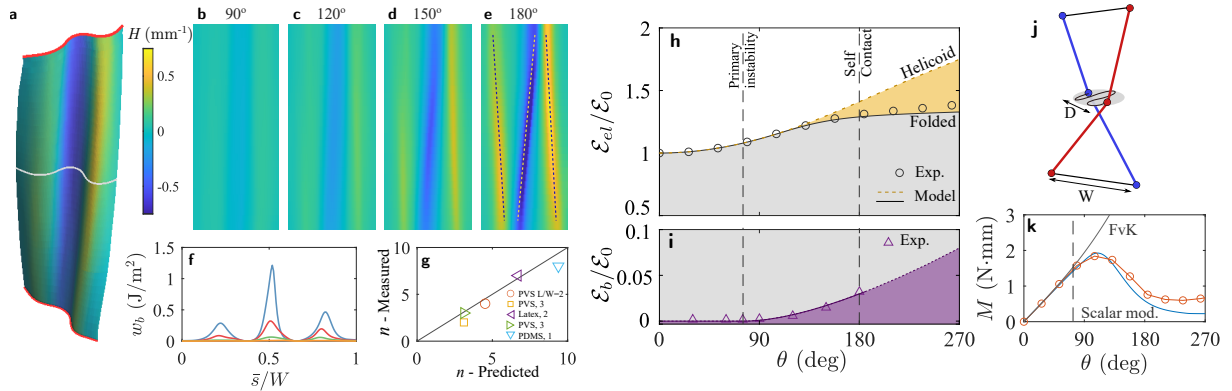


Figure 2: Curvature localization, stored elastic energy, and oscillating torque. (a) The deformation of a PVS sheet twisted by $\theta = 120^\circ$ obtained with x-ray tomography and rendered with mean curvature H given by color bar on right ($L/W = 3$; $t/W = 0.009$; $\theta_p = 75 \pm 5^\circ$). The central 80% of the sheet away from the clamps is shown. (b) to (e) The spatial distribution H mapped to a rectangular domain shows symmetry breaking and localization of the sheet curvature with twist. (f) Bending content w_b shows the localization of energy with creasing across the crosssection indicated by the solid white line in (a). (g) The measured number of folds n is in good agreement with the prediction $n = 2W/\lambda_p$. (h) Elastic energy \mathcal{E}_{el} obtained experimentally (circles) and from folded model and unbuckled helicoid scaled by \mathcal{E}_0 at zero twist. Elastic energy for $\chi = 1$ (helicoid case) is significantly higher for $\theta > 180^\circ$ (yellow dashed line). (i) The scaled bending energy $\mathcal{E}_b/\mathcal{E}_0$ (purple triangles) obtained by integrating the measured bending energy density is at least an order of magnitude lower than $\mathcal{E}_{el}/\mathcal{E}_0$. (j) Schematic illustrating the scalar model used to calculate the elastic energy stored in the sheet. (k) The oscillation of measured torque M (circles) versus θ is quantitatively captured by our scalar model (solid line), unlike the prediction from the FvK equations.

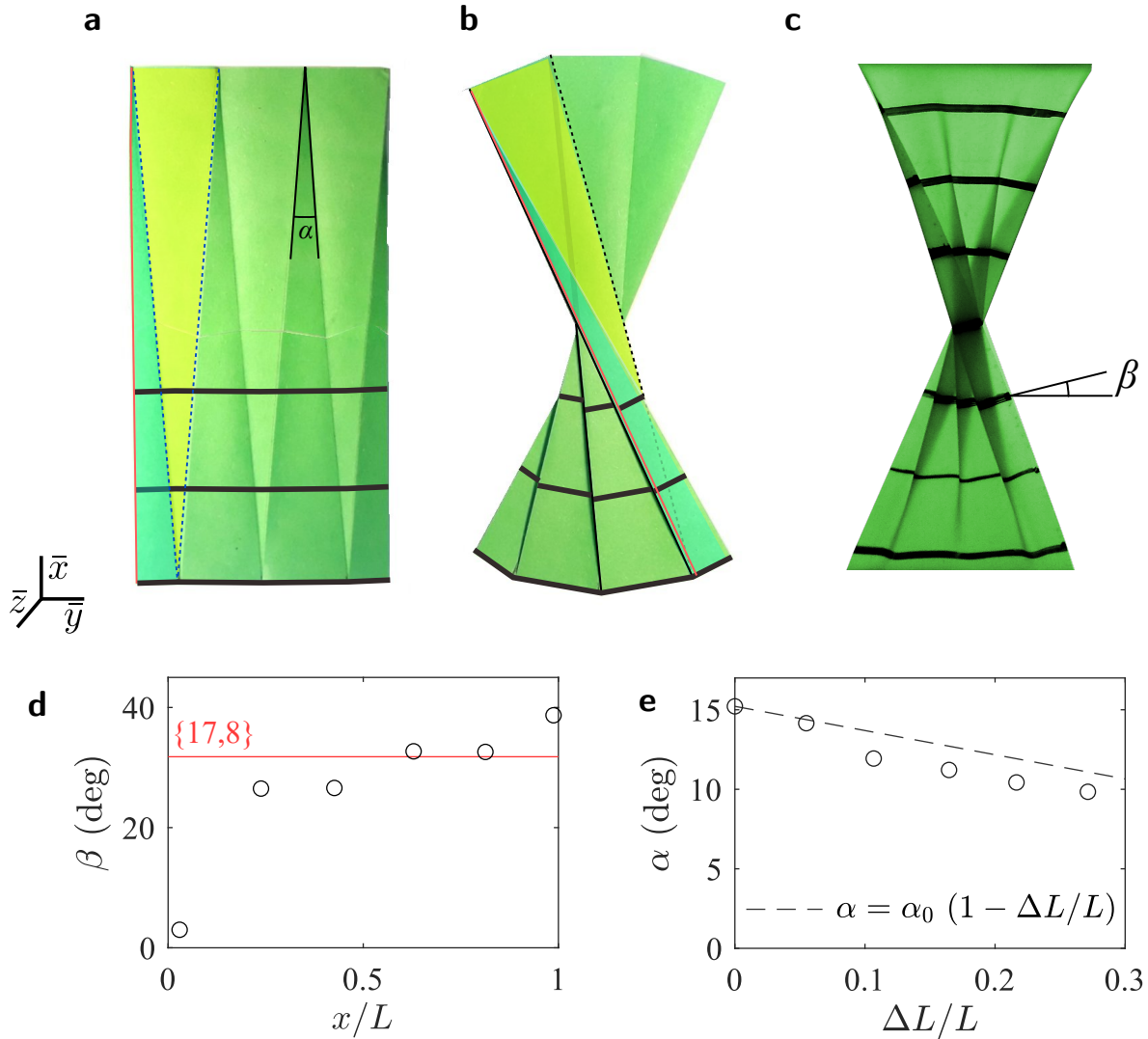


Figure 3: Half-twisted sheets fold like an origami away from the clamp. (a) Flat sheet with triangular up and down fold lines. Horizontal black solid line is drawn to indicate the relative displacement. (b) Corresponding origami with 6 flat folds. (c) Elastic sheet twisted by $\theta = 180^\circ$ shows similar fold structure away from the clamped edges. (d) The segment angle β as a function of distance across sheet width for elastic sheet and origami. Solid red line indicates the expected segment slope value $\beta = 31.8^\circ$ for an origami with the same tip angle α . (e) The angle α of stretched triangle as a function applied strain $\Delta L/L$.

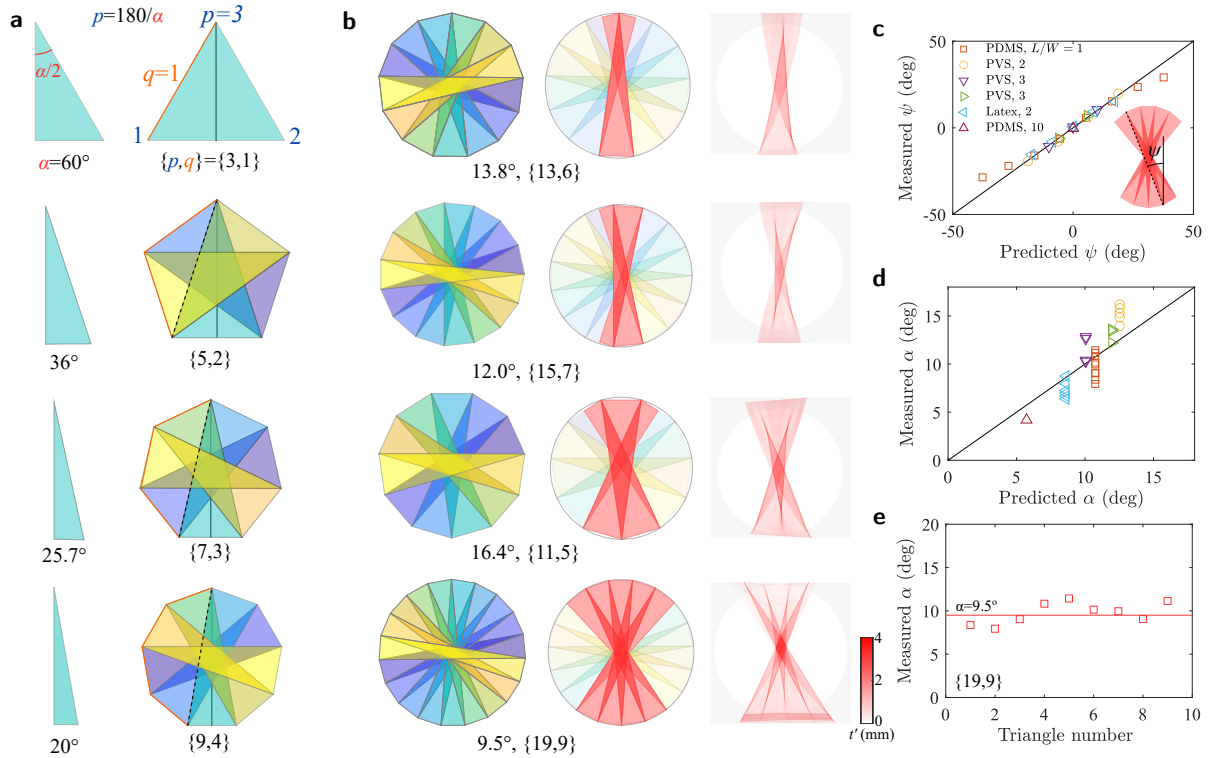


Figure 4: Partial Schläfli origami explains layered architectures at half-twist. (a) Geometrical forms obtained by increasing the Schläfli symbols and number of facets. (b) Comparison of the experimental radiogram and Schläfli fold origami. Good correspondence is observed in all four cases. (c) The edge angle as a function of the calculated angle using geometric model is in excellent agreement. (d) Comparison of the apex angle α as a function calculated α using various sheets and loading. (e) The tip angle as a function of fold number is essentially constant.

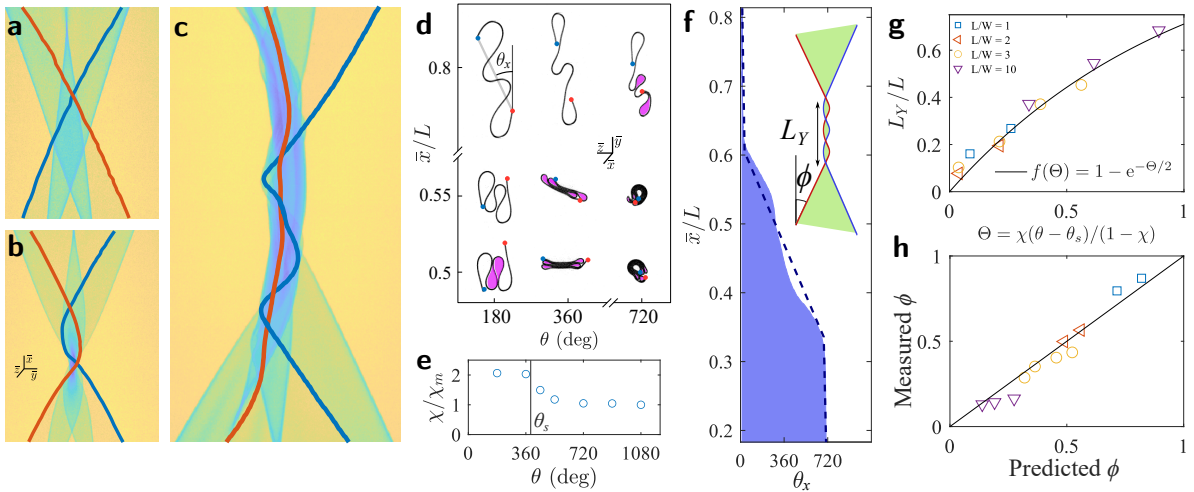


Figure 5: Topological transformation into architectured yarns through recursive folding and twist localization. (a to c) Fluoroscopy images corresponding to $\theta = 180^\circ, 360^\circ$, and 720° . (d) Crosssections at $x/L = 1, 1.1$ and 1.6 for twist angle $180^\circ, 360^\circ$, and 720° highlighting edges (red and blue disks) and encapsulated regions (magenta shades). (e) Compaction parameter shows a sharp decrease at the secondary instability. (f) The orientation angle of the edge θ_x versus \bar{x}/L . Inset: schematics of a sheet in the yarn regime. (g) The fraction of the yarn length L_Y/L versus Θ . (h) Measured angle subtended by the fan versus the prediction $\phi = (W - D)/(L - L_Y)$.